A high HDO/H2O ratio in the Class I protostar L1551 IRS5

A. Andreu, A. Coutens, F. Cruz-Sáenz de Miera, N. Houry, J. K. Jørgensen, A. Kóspál, D. Harsono

A&A 677, L17 (2023)
https://doi.org/10.1051/0004-6361/202347484

Astronomy & Astrophysics

LETTER TO THE EDITOR

A high HDO/H_2O ratio in the Class I protostar L1551 IRS5⋆

A. Andreu[1], A. Coutens[1], F. Cruz-Sáenz de Miera[1,2,3], N. Houry[1], J. K. Jørgensen[4], A. Kóspál[2,3,5,6], and D. Harsono[7]

[1] Institut de Recherche en Astrophysique et Planétologie (IRAP), Université de Toulouse, UT3-PS, CNRS, CNES, 9 av. du Colonel Roche, 31028 Toulouse Cedex 4, France
e-mail: audrey.andreu@irap.omp.eu; audrey.coutens@irap.omp.eu
[2] Konkoly Observatory, Research Centre for Astronomy and Earth Sciences, Eötvös Loránd Research Network (ELKH), Konkoly-Thege Miklós út 15-17, 1121 Budapest, Hungary
[3] CSFK, MTA Centre of Excellence, Budapest, Konkoly Thege Miklós út 15-17, 1121 Budapest, Hungary
[4] Centre for Star and Planet Formation, Niels Bohr Institute & Natural History Museum of Denmark, University of Copenhagen, Øster Voldgade 5-7, 1350 Copenhagen K, Denmark
[5] Max-Planck-Institut für Astronomie, Königstuhl 17, 69117 Heidelberg, Germany
[6] Eötvös Loránd University, Department of Astronomy, Pázmány Péter sétány 1/A, 1117 Budapest, Hungary
[7] Institute of Astronomy, Department of Physics, National Tsing Hua University, Hsinchu, Taiwan

Received 17 July 2023 / Accepted 29 August 2023

ABSTRACT

Context. Water is a very abundant molecule in star-forming regions. Its deuterium fractionation provides an important tool for understanding its formation and evolution during the star and planet formation processes. While the HDO/H_2O abundance ratio has been determined toward several young Class 0 protostars and comets, the number of studies toward Class I protostars is limited.
Aims. Our aim is to study the water deuteration toward the Class I protostellar binary L1551 IRS5 and to investigate the effect of evolutionary stage and environment on variations in the water D/H ratio.
Methods. Observations were carried out toward L1551 IRS5 using the NOrthern Extended Millimeter Array (NOEMA) interferometer. The HDO $3_{1,2}$–$2_{2,1}$ transition at 225.9 GHz and the $H_2{}^{18}O$ $3_{1,3}$–$2_{2,0}$ transition at 203.4 GHz were covered with a spatial resolution of 0.5″× 0.8″, while the HDO $4_{2,2}$–$4_{2,3}$ transition at 143.7 GHz was observed with a resolution of 2.0″ × 2.5″. We constrained the water D/H ratio using both local thermodynamic equilibrium (LTE) and non-LTE models.
Results. The three transitions are detected. The line profiles display two peaks, one at ∼6 km s^{-1} and one at ∼9 km s^{-1}. We derive an HDO/H_2O ratio of $(2.1 \pm 0.8) \times 10^{-3}$ for the redshifted component and a lower limit of $>0.3 \times 10^{-3}$ for the blueshifted component. This lower limit is due to the blending of the blueshifted $H_2{}^{18}O$ component with redshifted CH_3OCH_3 emission.
Conclusions. The HDO/H_2O ratio in L1551 IRS5 is similar to the values in Class 0 isolated sources and in the disk of the Class I protostar V883 Ori, while it is significantly higher than in the previously studied clustered Class 0 sources and the comets. This result suggests that the chemistry of protostars that belong to molecular clouds with relatively low source densities, such as L1551, share more similarities with the isolated sources than the protostars of very dense clusters. If the HDO/H_2O ratios in Class 0 protostars with few sources around are comparable to those found to date in isolated Class 0 objects, it would mean that there is little water reprocessing from the Class 0 to Class I protostellar stage.

Key words. astrochemistry – stars: protostars – stars: formation – ISM: molecules – ISM: individual objects: L1551 IRS5

1. Introduction

Water is one of the most abundant molecules in the interstellar medium. Its role is significant in the star formation process as it cools down the warm regions and boosts the gravitational collapse. It has been detected in multiple environments, such as protostars (e.g., van Dishoeck et al. 2021), protoplanetary disks (e.g., Hogerheijde et al. 2011), comets (e.g., Mumma et al. 1986; Davies et al. 1997), and asteroids (e.g., Rivkin & Emery 2010). Deuteration is extremely sensitive to density and temperature conditions (Ceccarelli et al. 2014), and higher D/H ratios are expected in particular when water forms in cold and dense conditions (e.g., Coutens et al. 2012; Jensen et al. 2019). The comparison of the D/H abundance ratio of the terrestrial oceans (Vienna Standard Mean Ocean Water (VSMOW) ∼ 1.557×10^{-4}, de Laeter et al. 2003) with comets and asteroids (a few 10^{-4}) suggests that these primitive objects could have delivered part of the water found on Earth (e.g., Hartogh et al. 2011; Altwegg et al. 2015; Trigo-Rodríguez et al. 2019). Chemical models of water deuteration in protoplanetary disks also show that the fractionation is not efficient enough to reproduce the terrestrial water D/H ratio without considering an inheritance from the parental molecular cloud (Cleeves et al. 2014). Studying the water deuteration in protostars can consequently help understand the origin of water in disks and planets (Furuya et al. 2016).

During the last decade the water deuterium fractionation ratio[1] has been measured in the warm inner regions of

⋆ This work is based on observations carried out under project numbers W18AO and S16AE with the IRAM NOEMA Interferometer. IRAM is supported by INSU/CNRS (France), MPG (Germany), and IGN (Spain).

[1] The D/H ratio of water is equal to 1/2 × HDO/H_2O due to statistics.

several Class 0 protostars, thanks to interferometric observations with the Atacama Large Millimeter/submillimeter Array (ALMA), the Submillimeter Array, and the Plateau de Bure Interferometer (Jørgensen & van Dishoeck 2010; Taquet et al. 2013; Coutens et al. 2014, and references thereafter). In the clustered sources (IRAS 16293−2422, NGC 1333 IRAS2A, IRAS4A−NW, and IRAS4B) the HDO/H_2O ratio was found to range between 6×10^{-4} and 19×10^{-4} (Persson et al. 2013, 2014). However, for the isolated sources (L483, B335, and BHR71−IRS1) Jensen et al. (2019) found a HDO/H_2O ratio of $(1.7–2.2)\times10^{-3}$, which is a factor of ∼2–4 higher than for the clustered sources. This difference was proposed to be the consequence of different durations or temperatures in the prestellar phase (Jensen et al. 2021).

To reconstruct the full history of water during the star formation process and bridge the gap between the Class 0 protostellar stage and the formation of planets, comets, and asteroids, studies of more evolved protostars are needed. Even if the detection of water is usually difficult in such sources (Harsono et al. 2020), there are a few Class I objects in which water can be detected, for example after a strong increase in the accretion rate from the disk onto the protostar (e.g., FUor or EXor sources, Audard et al. 2014; Fischer et al. 2022). Such an event leads to a luminosity burst that warms up the disk and the envelope in which the icy grain mantles can sublimate (Cieza et al. 2016). However, the studies were limited to only two sources. A first study by Codella et al. (2016) showed the detection of HDO toward the EXor-like source SVS13-A with the IRAM 30 m telescope. The presence of high-energy transitions suggests that they come from the warm inner regions even though emission from large-scale shocks cannot be excluded. From the nondetection of the $H_2{}^{18}O$ transition at 203.4 GHz, they estimated a lower limit of the HDO/H_2O ratio of $\gtrsim10^{-3}$. More recently, a HDO/H_2O ratio of $(2.26\pm0.63)\times10^{-3}$ was obtained with ALMA in the disk of the FUor protostar V883 Ori (Tobin et al. 2023). The similarity of the water deuteration in isolated Class 0 protostars supports the inheritance of water from the envelope to the disk.

Here we report the interferometric determination of the HDO/H_2O ratio in another Class I source, L1551 IRS5 (Chen et al. 1995). This protostellar binary, located in the Taurus molecular cloud (d ∼ 155 pc, Zucker et al. 2019), is classified as a FUor-like object by Connelley & Reipurth (2018) based on its near-infrared spectra (Mundt et al. 1985; Carr et al. 1987). The detection of complex organic molecules in its inner regions suggests high-temperature conditions that would be sufficient to thermally desorb the molecules frozen on grains, similarly to hot corinos (Bianchi et al. 2020; Cruz-Sáenz de Miera, in prep.).

2. Observations

Observations of two HDO transitions and one $H_2{}^{18}O$ transition were carried out toward L1551 IRS5 with the Northern Extended Millimeter Array (NOEMA) through the projects W18AO and S16AE (see Table 1). The HDO $3_{1,2}$–$2_{2,1}$ and $H_2{}^{18}O$ $3_{1,3}$–$2_{2,0}$ transitions at 225.9 GHz and 203.4 GHz, respectively, were observed simultaneously in the A configuration on 15 and 17 February 2019 and in the C configuration on 27 February 2019. High spectral resolution windows with channel spacing of 62.5 kHz (i.e., 0.08–0.09 km s^{-1}) were used to cover the two transitions. We resampled the data with a resolution dv of 0.5 km s^{-1} to increase the signal-to-noise ratio. The HDO $4_{2,2}$–$4_{2,3}$ transition at 143.7 GHz was covered with a poor resolution of 1.95 MHz (i.e., 4 km s^{-1}) in other NOEMA observations carried out on 25 August and 31 August 2016 in the D configuration. All the data were calibrated and imaged using the CLIC and MAPPING packages of the GILDAS[2] software. The list of calibrators for each observation is in Table A.1. The continuum was subtracted before the Fourier transform was applied to the line data. The data were imaged with the natural weighting mode. The synthesized beam sizes and rms obtained for each transition are listed in Table 1. The two components, N and S, of L1551 IRS5 are not fully resolved in our observations as they are only separated by 0.36″ (i.e., ∼56 AU, Cruz-Sáenz de Miera et al. 2019).

3. Results

In a first step, we visualized the datacubes of the HDO and $H_2{}^{18}O$ lines with the Aladin[3] and CASSIS[4] softwares (Bonnarel et al. 2000; Glorian et al. 2021). We extracted the spectra at the positions of the northern source ($\alpha_{J2000}=04^h31^m34\overset{s}{.}161$, $\delta_{J2000}=+18°08'04.72''$) and the southern source ($\alpha_{J2000}=04^h31^m34\overset{s}{.}165$, $\delta_{J2000}=+18°08'04.359''$, Takakuwa et al. 2020). To study variations in the line intensities with the position, the spectra were also extracted for a position between the two sources, at an equal distance from them ($\alpha_{J2000}=04^h31^m34\overset{s}{.}163$, $\delta_{J2000}=+18°08'04.550''$), that we call M. Because of the asymmetry in emission maps with respect to M, we include a position at a similar distance from N in the opposite direction ($\alpha_{J2000}=04^h31^m34\overset{s}{.}159$, $\delta_{J2000}=+18°08'04.890''$) called O. A comparison of these spectra is shown in Fig. 1, and their locations are indicated in Fig. 2.

Two velocity components are seen in the line profiles at 203.4 and 225.9 GHz, similarly to Bianchi et al. (2020) and Mercimek et al. (2022) for complex organic molecules. The component at ∼9 km s^{-1} is brighter at the N and O positions than at the M and S positions. The HDO component at ∼6 km s^{-1} is slightly brighter at the M position than the N and S positions, while it is less bright at the O position. The high-velocity peak corresponds to the N source or farther to the north, in agreement with Bianchi et al. (2020). The HDO component at 6 km s^{-1} seems to arise closer to the M position than the S position based on the comparison of the observed line intensities. The double peak created by these two velocity components could then possibly indicate rotation from a disk surrounding the N source. For the HDO line at 143.7 GHz, the spatial resolution is too low (∼2.0–2.5″) compared to the binary separation (0.36″) to observe spectral differences at the four positions (see Fig. 1). The two velocity components are not observed because of the low spectral resolution of the data (4 km s^{-1}).

We used the CASSIS software to check possible blending with other molecules at velocities of both 6 km s^{-1} and 9 km s^{-1}. The spectroscopic data come from the CDMS and JPL databases (Pickett et al. 1998; Müller et al. 2005). No blending is observed for the component at ∼9 km s^{-1} either for HDO or $H_2{}^{18}O$. However, the $H_2{}^{18}O$ component at ∼6 km s^{-1} is blended with a CH_3OCH_3 $3_{3,1,1}$–$2_{2,1,1}$ line emitted at ∼9 km s^{-1}. A faint line of CH_3OCHO $6_{6,0}$–$5_{5,0}$ (emission at 9 km s^{-1}) is observed in the wing of the HDO transition at 225.9 GHz. The HDO line at 143.7 GHz does not seem to be affected by blending.

Integrated emission maps of the HDO 225.9 GHz and $H_2{}^{18}O$ 203.4 GHz lines are shown in Fig. 2. The water emission is compact (less than 70 AU in diameter), as also seen for complex

[2] http://www.iram.fr/IRAMFR/GILDAS/
[3] https://aladin.u-strasbg.fr/AladinDesktop/
[4] CASSIS (http://cassis.irap.omp.eu/) has been developed by IRAP-UPS/CNRS.

Table 1. Detected HDO and $H_2{}^{18}O$ transitions toward the L1551 IRS5 source.

Molecule	Transition	Frequency [MHz]	E_{up} [K]	A_{ij} [s^{-1}]	g_{up}	Beam size [″ × ″]	PA [°]	rms [mJy beam^{-1}]	dv [km s^{-1}]	Project
HDO	$3_{1,2}$–$2_{2,1}$	225 896.72	168	1.3×10^{-5}	7	0.76 × 0.51	21.7	4.2	0.5	W18AO
$H_2{}^{18}O$	$3_{1,3}$–$2_{2,0}$	203 407.52	204	4.8×10^{-6}	7	0.83 × 0.57	24.0	3.7	0.5	W18AO
HDO	$4_{2,2}$–$4_{2,3}$	143 727.21	319	2.8×10^{-6}	9	2.51 × 2.05	37.1	2.1	4.0	S16AE

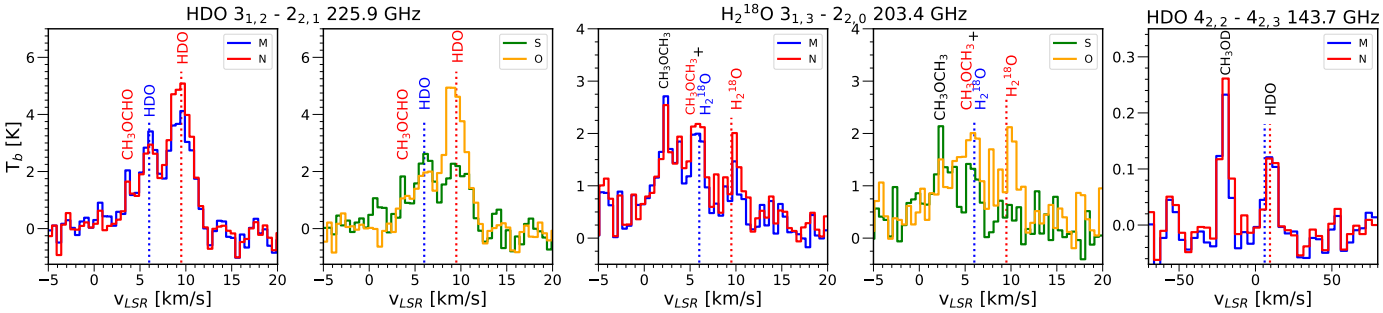

Fig. 1. Comparison of the spectra of the water isotopolog transitions. The green, blue, red, and orange solid lines represent the spectra extracted at the position S, M, N, and O, respectively. The dotted lines show velocities of 6.0 km s^{-1} (blue) and 9.5 km s^{-1} (red). Considering the synthetic beam sizes and the separation of the N and S components, the extracted spectra are not entirely independent from each other. For the HDO line at 143.7 GHz, the spatial resolution is too low to distinguish O from N and M from S. The x-axis scale is larger for this transition.

organic molecules (Bianchi et al. 2020). As expected, the HDO component at 9 km s^{-1} (in red) peaks close to the N position, while the one at 6 km s^{-1} (in blue) peaks closer to the M position. A similar distribution is seen for the $H_2{}^{18}O$ component at 9 km s^{-1}. However, the one at 6 km s^{-1} peaks closer to the N position. This can be explained by the blending with the CH_3OCH_3 line, which is emitted at a velocity of 9 km s^{-1}. It consequently means that the CH_3OCH_3 emission contributes significantly to the flux observed at 6 km s^{-1}. The HDO and $H_2{}^{18}O$ emission sizes were estimated with circular Gaussian fitting of the lines in the (u,v)-plane. We found approximate source sizes of 0.35″ and 0.45″ for the components at 6 and 9 km s^{-1}, respectively (see Table A.3).

To determine the water deuteration for the two velocity components, we used the HDO 225.9 GHz and $H_2{}^{18}O$ 203.4 GHz lines. We focused our analysis on the spectra extracted at the position of the N source for the component at 9 km s^{-1} and the spectra extracted at the position M (between N and S) for the component at 6 km s^{-1}. The line fluxes of the two components were collected by fitting the HDO and $H_2{}^{18}O$ lines with double Gaussian profiles with the Levenberg–Marquardt fitter (see Fig. A.1). The results of the fits are presented in Table A.2. Adding a third Gaussian for the CH_3OCHO peak does not affect the HDO flux within the uncertainties. The Gaussian fluxes also do not differ if we fix the same FWHM and v_{LSR} for the HDO and $H_2{}^{18}O$ lines. Based on the Gaussian fits, we calculated the column densities of each isotopolog assuming local thermodynamic equilibrium (LTE), following the formalism of Goldsmith et al. (1999) and Mangum & Shirley (2015). Then we derived the HDO/H_2O ratios assuming a $^{16}O/^{18}O$ ratio equal to 560 (Wilson & Rood 1994). We considered a range of excitation temperatures, T_{ex}, between 100 and 300 K, which are characteristic of hot corinos (e.g., Jørgensen et al. 2018). Source sizes of 0.35″ and 0.45″ were assumed for M and N, respectively. The lines are optically thin ($\tau \leq 0.23$ for HDO and $\tau \leq 0.15$ for $H_2{}^{18}O$) in both cases. Figure B.2 shows the variation in the HDO/H_2O ratio as a func-

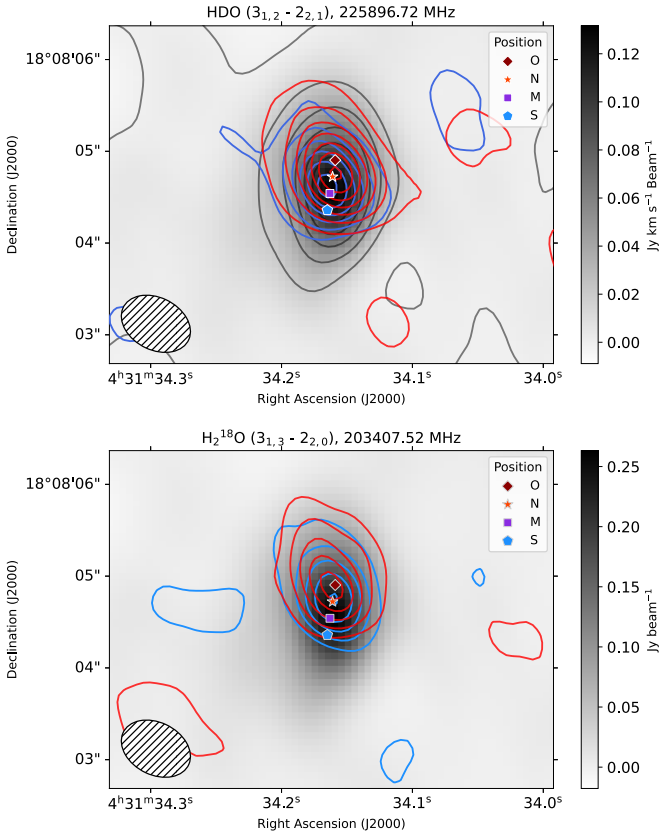

Fig. 2. Integrated emission maps of the HDO line at 225.9 GHz (top) and the $H_2{}^{18}O$ line at 203.4 GHz (bottom). The blue and red contours correspond to the integrated flux between 4.5 and 7.5 km s^{-1} and 7.5 and 12 km s^{-1}, respectively. The levels of contours start at 3σ with a step of 3σ for all except for the HDO contours in red (7.5–12 km s^{-1}) which are spaced by 5σ. Dust continuum is indicated in grayscale. The beam sizes are shown in the bottom left corner.

Table 2. Column densities and HDO/H_2O ratio in L1551 IRS5 for different excitation temperatures.

	Component 9 km s^{-1}, position N		Component 6 km s^{-1}, position M	
	T_{ex} = 100 K	T_{ex} = 300 K	T_{ex} = 100 K	T_{ex} = 300 K
	Column density [cm^{-2}]			
HDO	$(7.5 \pm 0.7) \times 10^{15}$	$(1.3 \pm 0.2) \times 10^{16}$	$(4.8 \pm 0.1) \times 10^{15}$	$(8.0 \pm 1.7) \times 10^{15}$
$H_2{}^{18}O$	$(8.4 \pm 2.5) \times 10^{15}$	$(1.1 \pm 0.3) \times 10^{16}$	$<(1.6 \pm 0.3) \times 10^{16}$	$<(2.1 \pm 0.4) \times 10^{16}$
	Isotopic ratio			
HDO/H_2O	$(1.6 \pm 0.6) \times 10^{-3}$	$(2.1 \pm 0.8) \times 10^{-3}$	$>(0.5 \pm 0.2) \times 10^{-3}$	$>(0.7 \pm 0.3) \times 10^{-3}$

Notes. The source sizes are assumed to be 0.35″ and 0.45″ for M and N, respectively. The error bars are based on the Gaussian fit uncertainties.

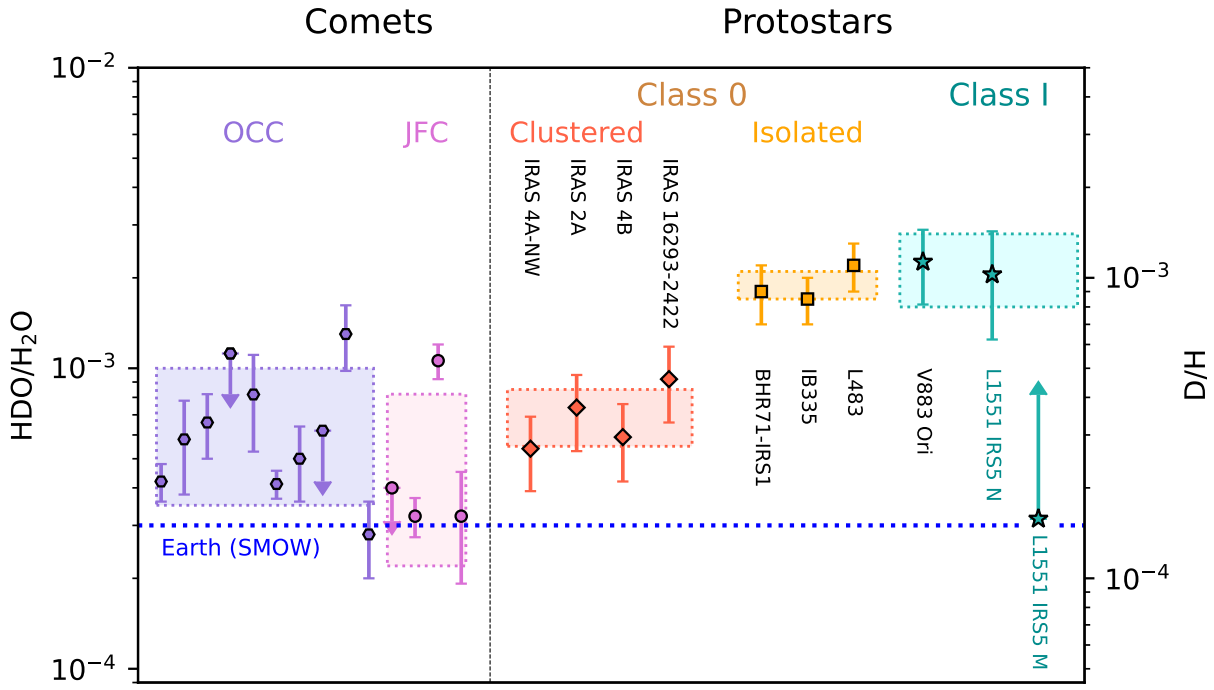

Fig. 3. Comparison of HDO/H_2O ratios in comets and protostars. The values and references can be found in Table C.1. The equivalent D/H ratio is indicated on the right axis. For L1551 IRS5 N ($v_{LSR} \sim 9$ km s^{-1}), the ratio is plotted for an excitation temperature of 300 K.

tion of the excitation temperature. The extreme values found for the HDO/H_2O ratio are listed in Table 2. The ratio varies between $(1.6 \pm 0.6) \times 10^{-3}$ and $(2.1 \pm 0.8) \times 10^{-3}$ for the component at 9 km s^{-1}. Only a lower limit of $>0.3 \times 10^{-3}$ can be derived for the component at 6 km s^{-1} given the blending of the $H_2{}^{18}O$ line with CH_3OCH_3. Using a different size does not significantly affect the HDO/H_2O ratio (see Appendix B.1). Non-LTE analysis also leads to similar results (see Appendix B.2).

As the fluxes of the two components at 6 and 9 km s^{-1} are not disentangled in the HDO observation at 143.7 GHz, we could not use it to derive the HDO/H_2O ratios. However, it can help us constrain the excitation temperatures of HDO. The analysis described in Appendix B.3 shows that a model with an excitation temperature for N equal to or lower than 220 K cannot reproduce the flux of the 143.7 GHz line within 20%. The HDO/H_2O ratio derived for T_{ex} = 300 K should consequently be considered more reliable than the value obtained for T_{ex} = 100 K.

4. Discussion

Figure 3 shows a comparison of the HDO/H_2O ratio of L1551 IRS5 with the values previously found in protostars and comets. For the component at 9 km s^{-1}, the HDO/H_2O ratio is similar to those measured in isolated Class 0 protostars (Jensen et al. 2019) and in the disk of the Class I V883 Ori (Tobin et al. 2023), and significantly higher than the previously studied clustered sources. At 6 km s^{-1}, the lower limit does not provide sufficient constraints to discriminate between the two categories.

Water observed in the warm inner regions of protostellar objects results from the thermal desorption of the icy grain mantles. Deuteration takes place early in the star formation process when the temperature is low and the density is relatively high. As a result, the gas phase HDO/H_2O ratio observed in the warm regions of Class 0 objects should reflect those of the icy grain mantles. Consequently, the observed deuterium fractionation ratio at the Class I stage should either be similar to the Class 0 stage or decrease if water is partially reprocessed in the hot corino. In the latter case the deuteration process would not be efficient enough to increase or maintain the overall deuteration level. From the HDO/H_2O ratio found in the high-velocity component of L1551 IRS5 we can conclude that the HDO/H_2O ratio does not decrease and is still quite high, similarly to what is found for V883 Ori (Tobin et al. 2023) and SVS13-A (Codella et al. 2016).

A second conclusion is that the chemistry of L1551 IRS5 appears to be closer to isolated sources than to clustered sources. The similarity with isolated sources can be surprising at first sight, as L1551 IRS5 is part of the Taurus molecular cloud. However, it is located in the LDN 1551 group in the southern part of the cloud (e.g., Roccatagliata et al. 2020). This group shows a lower density of sources than other regions in Taurus (Gomez et al. 1993). The spatial density of sources in the Taurus molecular cloud is also much lower (only a few tens in $\sim$1 pc^3, Gomez et al. 1993) than in Ophiuchus, which contains IRAS 16293−2422, and the NGC 1333 cloud in Perseus (a few 10^2–10^3, Bontemps et al. 2001; Jørgensen et al. 2006). As explained in Jensen et al. (2021), the higher water deuteration in isolated sources would be due to either a lower temperature or a longer prestellar phase compared to clustered sources. The environment around L1551 IRS5 could be colder than around IRAS 16293 and the NGC 1333 sources. The dense cores could also have more time to evolve before their collapse if L1551 IRS5 is on the edge of the cloud and if it is surrounded by fewer sources. As a consequence, the water deuteration in L1551 IRS5 would be closer to the Class 0 isolated sources. A similar explanation was proposed for the Class I protostar V883 Ori, which belongs to the Orion molecular cloud, but is in a relatively isolated area (Tobin et al. 2023). The lower values found in comets and in the protostars IRAS 16293−2422, NGC 1333 IRAS2A, IRAS4A, and IRAS4B suggest that our Solar System formed in a relatively dense clustered area. The similarity of the HDO/H_2O ratio between the binary L1551 IRS5 and the singly Class I object V883 Ori also seems to indicate that the binarity does not influence the water deuteration.

In conclusion, this study highlights the importance of carrying out water deuteration measurements toward more sources, at different evolutionary stages, and in different environments in order to better understand the water formation and evolution during the formation process of solar-type stars. Investigations of the D_2O/HDO ratio in Class I protostars would also be useful to check the similarity with Class 0 sources.

Acknowledgements. The authors thank the IRAM staff, especially Jan Martin Winters and Jérémie Boissier for their help with the data reduction. This study is part of a project that has received funding from the European Research Council (ERC) under the European Union's Horizon 2020 research and innovation programme under Grant agreement No. 949278 (Chemtrip) and Grant agreement No. 716155 (SACCRED). This work made use of Astropy: (http://www.astropy.org) a community-developed core Python package and an ecosystem of tools and resources for astronomy (Astropy Collaboration 2013, 2018, 2022).

References

Altwegg, K., Balsiger, H., Bar-Nun, A., et al. 2015, Science, 347, 1261952P
Astropy Collaboration (Robitaille, T. P., et al.) 2013, A&A, 558, A33
Astropy Collaboration (Price-Whelan, A. M., et al.) 2018, AJ, 156, 123
Astropy Collaboration (Price-Whelan, A. M., et al.) 2022, ApJ, 935, 167
Audard, M., Ábrahám, P., Dunham, M. M., et al. 2014, in Protostars and Planets VI, eds. H. Beuther, R. S. Klessen, C. P. Dullemond, & T. Henning, 387
Bianchi, E., Chandler, C. J., Ceccarelli, C., et al. 2020, MNRAS, 498, L87
Biver, N., Bockelée-Morvan, D., Crovisier, J., et al. 2006, A&A, 449, 1255
Biver, N., Moreno, R., Bockelée-Morvan, D., et al. 2016, A&A, 589, A78
Bockelée-Morvan, D., Gautier, D., Lis, D. C., et al. 1998, Icarus, 133, 147
Bockelée-Morvan, D., Biver, N., Swinyard, B., et al. 2012, A&A, 544, L15
Bonnarel, F., Fernique, P., Bienaymé, O., et al. 2000, A&AS, 143, 33
Bontemps, S., André, P., Kaas, A. A., et al. 2001, A&A, 372, 173
Brown, R. H., Lauretta, D. S., Schmidt, B., & Moores, J. 2012, Planet. Space Sci., 60, 166
Carr, J. S., Harvey, P. M., & Lester, D. F. 1987, ApJ, 321, L71
Ceccarelli, C., Caselli, P., Bockelée-Morvan, D., et al. 2014, in Protostars and Planets VI, eds. H. Beuther, R. S. Klessen, C. P. Dullemond, & T. Henning, 859
Chen, H., Myers, P. C., Ladd, E. F., & Wood, D. O. S. 1995, ApJ, 445, 377
Cieza, L. A., Casassus, S., Tobin, J., et al. 2016, Nature, 535, 258
Cleeves, L. I., Bergin, E. A., Alexander, C. M. O. D., et al. 2014, Science, 345, 1590
Codella, C., Ceccarelli, C., Bianchi, E., et al. 2016, MNRAS, 462, L75
Connelley, M. S., & Reipurth, B. 2018, ApJ, 861, 145
Coutens, A., Vastel, C., Caux, E., et al. 2012, A&A, 539, A132
Coutens, A., Jørgensen, J. K., Persson, M. V., et al. 2014, ApJ, 792, L5
Cruz-Sáenz de Miera, F., Kóspál, Á., Ábrahám, P., Liu, H. B., & Takami, M. 2019, ApJ, 882, L4
Davies, J. K., Roush, T. L., Cruikshank, D. P., et al. 1997, Icarus, 127, 238
de Laeter, J. R., Böhlke, J. K., Bièvre, P. D., et al. 2003, Pure Appl. Chem., 75, 683
Fischer, W. J., Hillenbrand, L. A., Herczeg, G. J., et al. 2022, arXiv e-prints [arXiv:2203.11257]
Furuya, K., van Dishoeck, E. F., & Aikawa, Y. 2016, A&A, 586, A127
Gibb, E. L., Bonev, B. P., Villanueva, G., et al. 2012, ApJ, 750, 102
Glorian, J.-M., Fernique, P., Allen, M., et al. 2021, in ADASS XXXI Conference Oct 2021 (Cape Town: ASP), ASP Conf. Ser.
Goldsmith, P. F., Langer, W. D., & Velusamy, T. 1999, ApJ, 519, L173
Gomez, M., Hartmann, L., Kenyon, S. J., & Hewett, R. 1993, AJ, 105, 1927
Harsono, D., Persson, M. V., Ramos, A., et al. 2020, A&A, 636, A26
Hartogh, P., Lis, D. C., Bockelée-Morvan, D., et al. 2011, Nature, 478, 218
Hogerheijde, M. R., Bergin, E. A., Brinch, C., et al. 2011, Science, 334, 338
Hutsemékers, D., Manfroid, J., Jehin, E., Zucconi, J. M., & Arpigny, C. 2008, A&A, 490, L31
Jensen, S. S., Jørgensen, J. K., Kristensen, L. E., et al. 2019, A&A, 631, A25
Jensen, S. S., Jørgensen, J. K., Furuya, K., Haugbølle, T., & Aikawa, Y. 2021, A&A, 649, A66
Jørgensen, J. K., & van Dishoeck, E. F. 2010, ApJ, 725, L172
Jørgensen, J. K., Harvey, P. M., Evans, Neal J., I., , et al. 2006, ApJ, 645, 1246
Jørgensen, J. K., Müller, H. S. P., Calcutt, H., et al. 2018, A&A, 620, A170
Lis, D. C., Biver, N., Bockelée-Morvan, D., et al. 2013, ApJ, 774, L3
Lis, D. C., Bockelée-Morvan, D., Güsten, R., et al. 2019, A&A, 625, L5
Mangum, J. G., & Shirley, Y. L. 2015, PASP, 127, 266
Meier, R., Owen, T. C., Matthews, H. E., et al. 1998, Science, 279, 842
Mercimek, S., Codella, C., Podio, L., et al. 2022, A&A, 659, A67
Müller, H. S. P., Schlöder, F., Stutzki, J., & Winnewisser, G. 2005, J. Mol. Struc., 742, 215
Mumma, M. J., Weaver, H. A., Larson, H. P., Davis, D. S., & Williams, M. 1986, Science, 232, 1523
Mundt, R., Stocke, J., Strom, S. E., Strom, K. M., & Anderson, E. R. 1985, ApJ, 297, L41
Persson, M. V., Jørgensen, J. K., & van Dishoeck, E. F. 2013, A&A, 549, L3
Persson, M. V., Jørgensen, J. K., van Dishoeck, E. F., & Harsono, D. 2014, A&A, 563, A74
Pickett, H. M., Poynter, R. L., Cohen, E. A., et al. 1998, J. Quant. Spectr. Radiat. Transf., 60, 883
Rivkin, A. S., & Emery, J. P. 2010, Nature, 464, 1322
Roccatagliata, V., Franciosini, E., Sacco, G. G., Randich, S., & Sicilia-Aguilar, A. 2020, A&A, 638, A85
Takakuwa, S., Saigo, K., Matsumoto, T., et al. 2020, ApJ, 898, 10
Taquet, V., López-Sepulcre, A., Ceccarelli, C., et al. 2013, ApJ, 768, L29
Tobin, J. J., van't Hoff, M. L. R., Leemker, M., et al. 2023, Nature, 615, 227
Trigo-Rodríguez, J. M., Rimola, A., Tanbakouei, S., Soto, V. C., & Lee, M. 2019, Space Sci. Rev., 215, 18
van der Tak, F. F. S., Black, J. H., Schöier, F. L., Jansen, D. J., & van Dishoeck, E. F. 2007, A&A, 468, 627
van Dishoeck, E. F., Kristensen, L. E., Mottram, J. C., et al. 2021, A&A, 648, A24
Villanueva, G. L., Mumma, M. J., Bonev, B. P., et al. 2009, ApJ, 690, L5
Wilson, T. L., & Rood, R. 1994, ARA&A, 32, 191
Zucker, C., Speagle, J. S., Schlafly, E. F., et al. 2019, ApJ, 879, 125

Appendix A: Additional tables and figures on observations

Table A.1 lists the calibrators used for the different observations. Gaussian fitting was performed on the spectra to extract the fluxes of the HDO and $H_2{}^{18}O$ lines (see Figure A.1). A summary of the fit results is presented in Table A.2. We also performed circular Gaussian fitting of the emission lines in the (u,v)-plane to estimate the size of the sources. The results of the fits are summarized in Table A.3.

Table A.1. List of calibrators.

Project	Date	Configuration	Phase calibrators	Bandpass calibrator	Flux scale calibrator
W18AO	15 February 2019	A	0507+179, 0446+112	3C84	LkHα 101
W18AO	17 February 2019	A	0507+179, 0446+112	3C84	LkHα 101, 2013+370
W18AO	27 February 2019	C	0507+179, 0446+112	3C84	LkHα 101
S16AE	25 August 2016	D	0507+179, 0354+231	3C454.3	MWC349
S16AE	31 August 2016	D	0507+179, 0354+231	3C454.3	LkHα 101

Table A.2. Gaussian fitting parameters and fluxes of the water isotopolog lines.

Molecule	Rest frequency [MHz]	v_{LSR} [km s^{-1}]	Peak intensity [K]	FWHM [km s^{-1}]	Flux [K.km s^{-1}]
North source position (N)					
HDO	225 896.72	9.11 ± 0.06	5.22 ± 0.19	2.78 ± 0.15	15.46 ± 1.41
		5.71 ± 0.09	2.90 ± 0.23	1.96 ± 0.28	6.06 ± 1.34
$H_2{}^{18}O$	203 407.52	9.71 ± 0.15	1.61 ± 0.21	2.25 ± 0.38	3.85 ± 1.16
		5.44 ± 0.14	2.22 ± 0.21	2.71 ± 0.48	6.39 ± 1.73
Middle position (M)					
HDO	225 896.72	5.73 ± 0.10	3.20 ± 0.25	2.01 ± 0.26	6.87 ± 1.43
		9.15 ± 0.09	4.06 ± 0.21	2.89 ± 0.23	12.48 ± 1.67
$H_2{}^{18}O$	203 407.52	5.46 ± 0.09	2.06 ± 0.17	2.31 ± 0.26	5.07 ± 0.98
		9.54 ± 0.16	1.18 ± 0.17	2.29 ± 0.43	2.87 ± 0.96
N and M positions[(a)]					
HDO	143 727.21				1.07 ± 0.30

Notes. [(a)] The two components at 6 and 9 km s^{-1} cannot be distinguished because of the poor spectral resolution of the data (1.95 MHz). The total integrated flux is consequently only given for this transition. A similar flux is obtained for the N and M positions because of the low spatial resolution of the data (2.5″ × 2.1″).

Table A.3. Results from the circular Gaussian fits performed in the (u,v)-plane.

Transition	R.A.	Dec	FWHP [″]
HDO 225 GHz 6.7 - 12 km s^{-1}	$04^h31^m34\overset{s}{.}158$ (0.007)	+18°08′04.75 (0.01)	0.45 (0.02)
$H_2^{18}O$ 203 GHz 6.7 - 11 km s^{-1}	$04^h31^m34\overset{s}{.}155$ (0.044)	+18°08′04.80 (0.05)	0.45 (0.11)
HDO 225 GHz 3 - 7.3 km s^{-1}	$04^h31^m34\overset{s}{.}162$ (0.014)	+18°08′04.60 (0.02)	0.35 (0.04)

Notes. The uncertainties are indicated in parentheses.

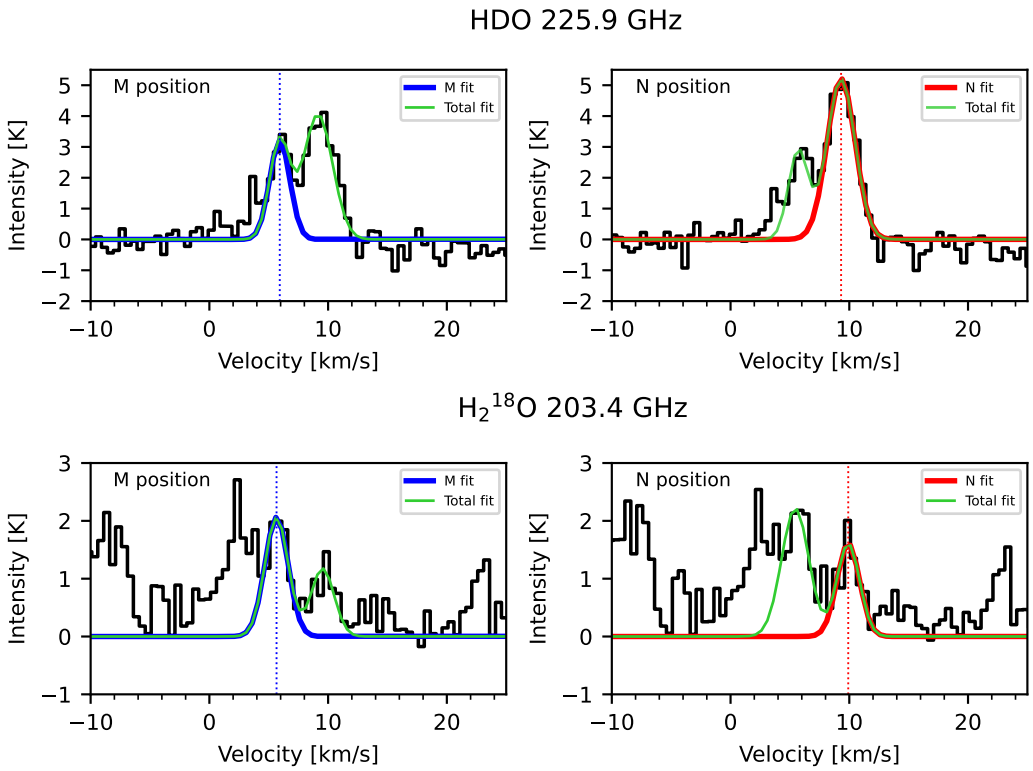

Fig. A.1. Gaussian line fits using the CASSIS software. The upper panel shows the spectra of the HDO transition at 225.9 GHz, while the lower panel is for the $H_2{}^{18}O$ transition at 203.4 GHz. The left plots are for the M position with the fit of the component at 6 km s^{-1} (blue), while the right plots are for the N position with the fit of the component at 9 km s^{-1} (red). The dotted lines indicate the central velocity of the respective Gaussian. The green line shows the corresponding double-Gaussian profiles (see Table A.2).

Appendix B: Exploration of the physical parameters and the LTE assumption

B.1. Impact of source size and excitation temperature on HDO/H_2O ratio

To investigate the impact of source size and excitation temperature on the HDO/H_2O ratio derived for the component at 9 km s^{-1}, we calculated the column densities needed to reproduce the fluxes of the HDO line at 225.9 GHz and the $H_2{}^{18}O$ line at 203.4 GHz for a wide range of excitation temperatures (100–300 K) and sizes (0.10–0.75″). The results of this method, which assumes LTE and optically thin lines, are presented in Figure B.1. The derived HDO/H_2O ratio is not very sensitive to the excitation temperature and size as it ranges between 1.5×10^{-3} and 2.2×10^{-3}. An analogous study done by Jørgensen & van Dishoeck (2010) led to similar conclusions.

Figure B.2 shows how the HDO/H_2O ratios of both components vary as a function of the excitation temperature when using the source sizes derived with circular Gaussian fitting of the lines in the (u,v)-plane.

B.2. Non-LTE modeling

The LTE assumption has been tested and approved for the same transitions in other hot corinos (Persson et al. 2014; Coutens et al. 2014). We carried out a similar test for L1551 IRS5 using the non-LTE radiative transfer code RADEX (van der Tak et al. 2007) with the Large Velocity Gradient (LVG) expanding sphere method. We varied the temperature between 100 and 300 K, similarly to the LTE analysis. For the H_2 density, we considered a range from 10^7 to 10^{11} cm^{-3}. With a non-LTE analysis of three HDO lines, Coutens et al. (2014) derived a H_2 density higher than 10^8 cm^{-3} in the warm inner regions of the low-mass protostar NGC1333 IRAS2A. The results are shown in Figure B.3. The HDO/H_2O ratio derived with RADEX, (1.3 - 1.8) $\times 10^{-3}$ is in agreement with the LTE values within the uncertainties.

B.3. Modeling of the HDO line at 143.7 GHz and constraints on the excitation temperatures

The spectral resolution of the HDO transition at 143.7 GHz does not allow us to distinguish between the fluxes coming from the component at 6 km s^{-1} and the one at 9 km s^{-1}. However, we can use the total flux to constrain the excitation temperatures for the two components. Assuming the source sizes obtained with the fits in the (u,v)-plane, we calculated the column densities of HDO needed to reproduce the two components at 225.9 GHz for various excitation temperatures. Then we predicted the expected flux at 143.7 GHz at 6 and 9 km s^{-1}, and summed the two fluxes before comparing them to the observed flux (see Table A.2). Figure B.4 shows that a good agreement (< 20%) is only found if the excitation temperature for the component at 9 km s^{-1} is $\gtrsim$ 240 K. The excitation temperature is not constrained for the component at 6 km s^{-1}.

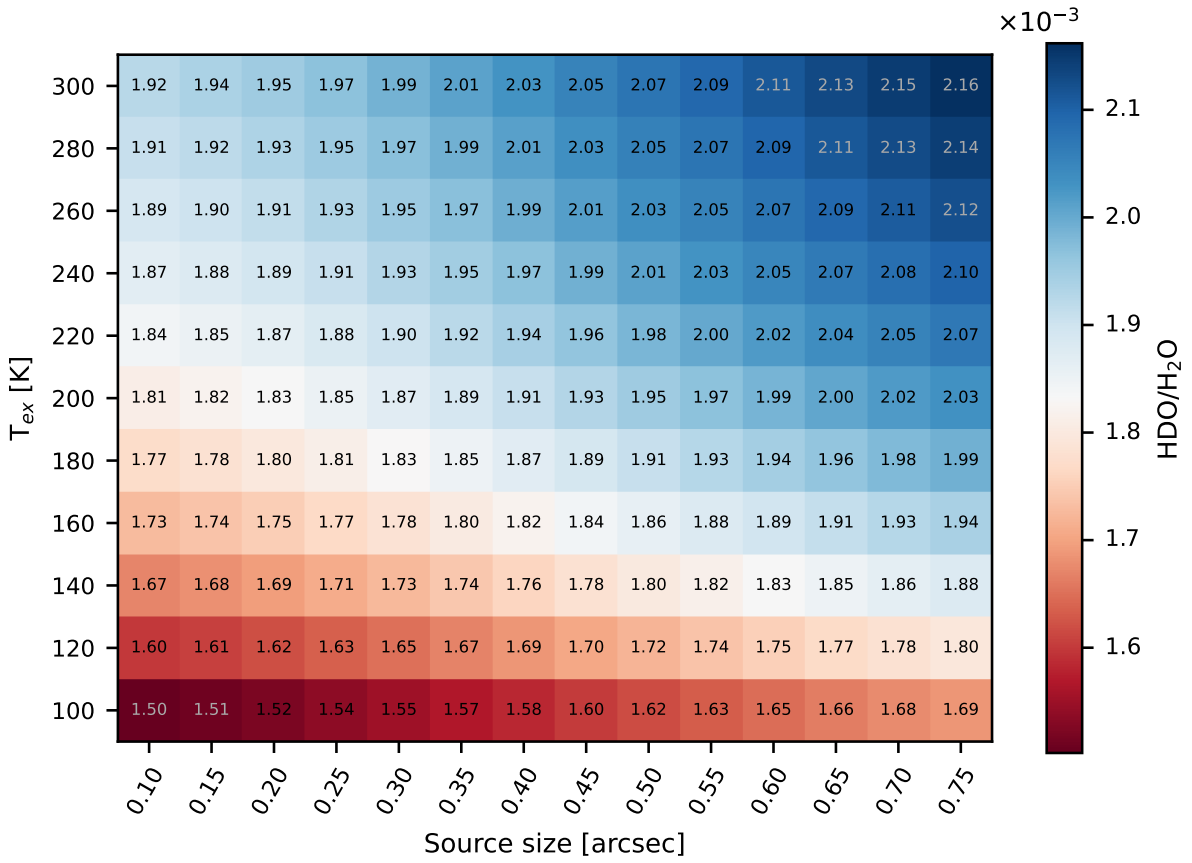

Fig. B.1. HDO/H_2O ratios ($\times 10^{-3}$) obtained for the component at 9 km s^{-1} (N) of L1551 IRS5 as a function of different excitation temperatures and sizes assuming optically thin LTE emission.

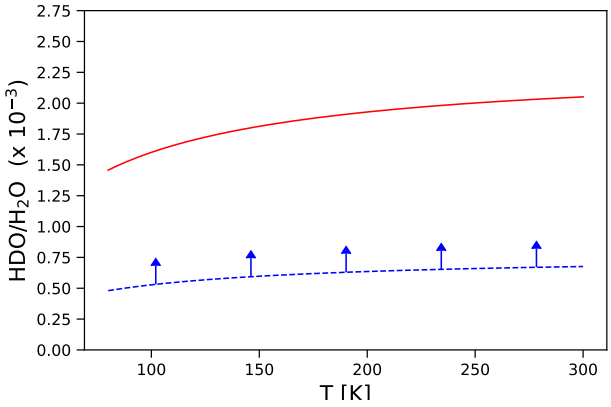

Fig. B.2. Evolution of HDO/H_2O ratio as a function of excitation temperature assuming source sizes of 0.35″ and 0.45″ for the M and N positions, respectively. The solid red line represents the ratio found for N (component at 9 km s^{-1}), while the blue dashed line is for M (6 km s^{-1}). The arrows indicate lower limits.

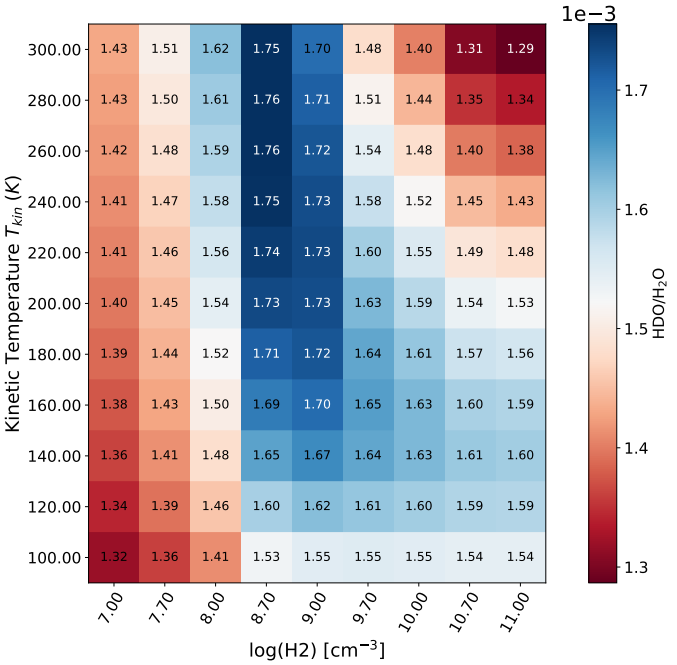

Fig. B.3. HDO/H_2O ratio ($\times$ 10^{-3}) obtained for the component at 9 km s^{-1} (N) of L1551 IRS5 with the non-LTE radiative transfer code RADEX as a function of the kinetic temperature and the H_2 density.

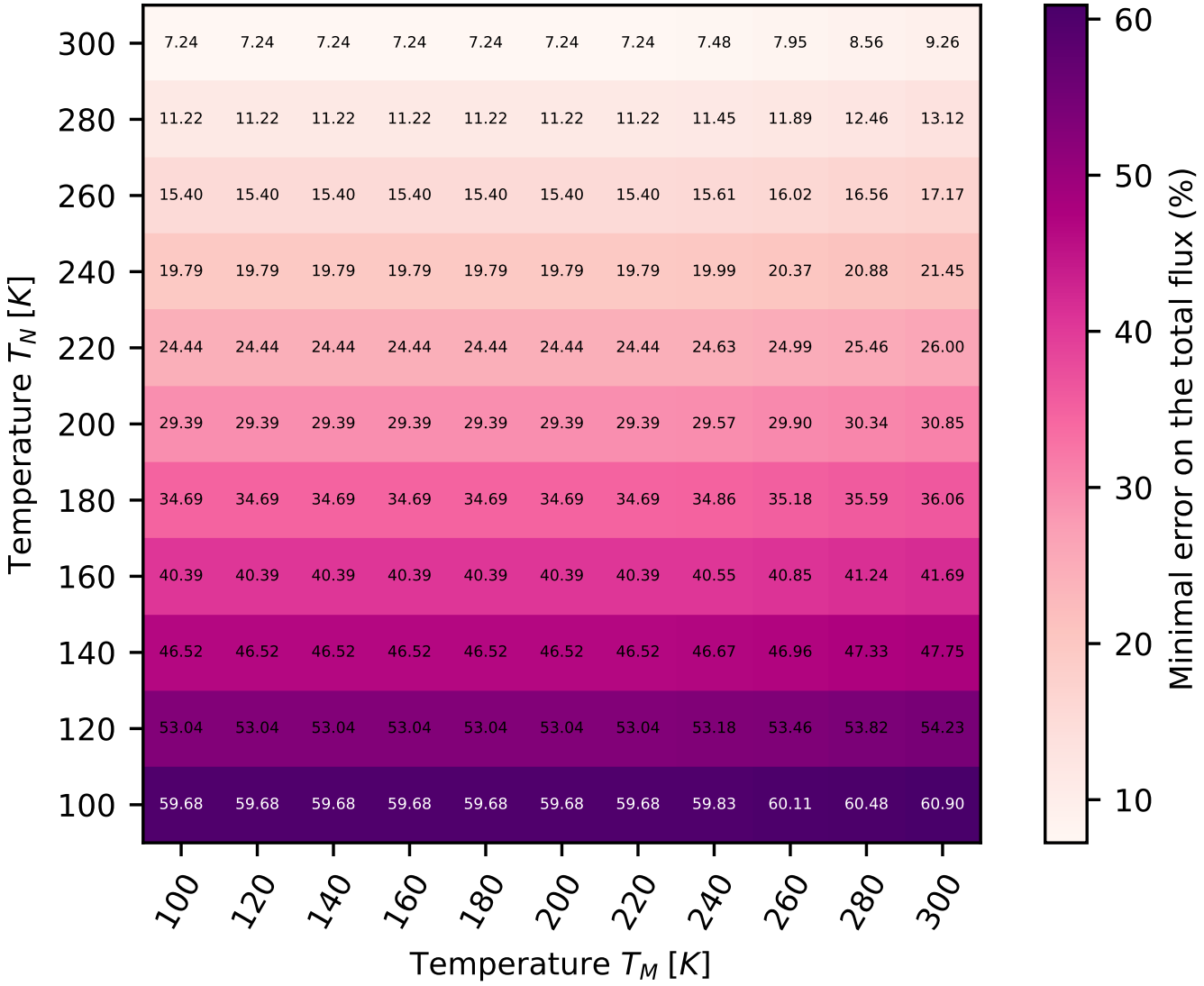

Fig. B.4. Percentage errors between the predicted and observed fluxes of the HDO line at 143.7 GHz as a function of excitation temperature for positions M and N. Source sizes of 0.35″ and 0.45″ are assumed for the M and N positions, respectively.

Appendix C: Previous results on water deuteration

Table C.1 summarizes the HDO/H_2O ratios determined in comets and protostars.

Table C.1. Water deuterium fractionation ratios determined in comets and protostars.

Source name	HDO/H_2O ($\times 10^{-4}$)	Ref.
Oort Cloud Comets		
1/P Halley	4.2 ± 0.6	(1)
C/1996 B2 Hyatuake	5.8 ± 2.0	(2)
C/1995 O1 Hale-Bopp	6.6 ± 1.6	(3)
C/2007 B3 Lulin	< 11.2	(4)
8P/Tuttle	8.2 ± 2.9	(5)
C/2009 P1 Garradd	4.1 ± 0.4	(6)
C/2002 T7 LINEAR	5.0 ± 1.4	(7)
153P Ikeya-Zhang	< (5.6 ± 0.6)	(8)
C/2012 F6 Lemmon	13.0 ± 3.2	(9)
CC/2014 Q2 Lovejoy	2.8 ± 0.8	(9)
Jupiter Family Comets		
45P/Honda-Mrkos-Pajdušáková	< 4.0	(10)
103P Hartley 2	3.2 ± 0.5	(11)
67/P Churyumov-Gerasimenko	10.6 ± 1.4	(12)
46P/Wirtanen	3.2 ± 1.3	(13)
Clustered Class 0 protostars		
NGC1333 IRAS 4A-NW	5.4 ± 1.5	(14)
NGC1333 IRAS 2A	7.4 ± 2.1	(14)
NGC1333 IRAS 4B	5.9 ± 2.6	(14)
IRAS 16293-2422	9.2 ± 2.6	(15)
Isolated Class 0 protostars		
BHR71-IRS1	18 ± 4	(16)
B335	17 ± 3	(16)
L483	22 ± 4	(16)
Class I protostars		
V883 Ori	23 ± 6	(17)
L1551 IRS5 – N, $v_{LSR} \sim 9$ km s^{-1}	21 ± 8	(18)
L1551 IRS5 – M, $v_{LSR} \sim 6$ km s^{-1}	> (5 ± 2)	(18)

Notes. This table is an updated version of Table A1 from Jensen et al. (2019). A factor 2 error on the conversion of the D/H ratio onto the HDO/H_2O ratio has been corrected for the comets C/2012 F6 Lemmon and CC/2014 Q2 Lovejoy (Biver et al. 2016). **References.** (1) Brown et al. (2012); (2) Bockelée-Morvan et al. (1998); (3) Meier et al. (1998); (4) Gibb et al. (2012); (5) Villanueva et al. (2009); (6) Bockelée-Morvan et al. (2012); (7) Hutsemékers et al. (2008); (8) Biver et al. (2006); (9) Biver et al. (2016); (10) Lis et al. (2013); (11) Hartogh et al. (2011); (12) Altwegg et al. (2015); (13) Lis et al. (2019); (14) Persson et al. (2014); (15) Persson et al. (2013); (16) Jensen et al. (2019); (17) Tobin et al. (2023); (18) This work.